Analysis of Intermediate State Ferroelectric Properties of 30% ScAlN, Impacts on Piezoelectric Performance, and Ferroelectric Dead Layer Effect in PMUT Devices

Sean J.Z. Wong, Chen Liu, Yan Hong, Muhammad Usman Khan, *Student Member, IEEE*, Chengkuo Lee*, Senior Member, IEEE,* Alessandro Stuart Savoia, *Member, IEEE, and* Yao Zhu, *Member, IEEE*

***Abstract*—The ferroelectricity of scandium-doped aluminium nitride (ScAlN) provides important advantages, such as control over the direction of electromechanical response, over traditional aluminium nitride used commonly in piezoelectric micromachined ultrasound transducers (PMUTs). Current literature surrounding the effect of intermediate polarization states on the piezoelectric properties of ferroelectric PMUT devices is limited, and this paper provides an experimentally obtained catalogue of the intermediate polarization states between the as-deposited N-polar and oppositely switched Al-polar states, comments on the polarization magnitudes and subsequent impact on PMUT resonant frequency and electromechanical coupling coefficient k_{eff}^2 and observes an asymmetrical response between the two saturated polarization states. It is found that the device polarized in the N-polar direction features improved k_{eff}^2, exhibiting a V-shaped response over polarization magnitude, with poorer performance in the fully Al-polar direction. The existence of a ferroelectrically dead layer within the ScAlN film, which retains its piezoelectric properties but is unable to be ferroelectrically switched, is experimentally examined. By comparison with finite-element simulations, a model containing a fixed N-polar dead layer equivalent to approximately 10% of the ScAlN film thickness and located at the bottom interface provides the closest agreement with the measured polarization and k_{eff}^2 asymmetries. The estimated thickness and location are obtained from device-level measurements and model comparison rather than direct structural characterization. Additionally, the propagation of the ferroelectric switching through the intermediate states is shown to be axial (thickness direction) in nature, matching well with previous research.**

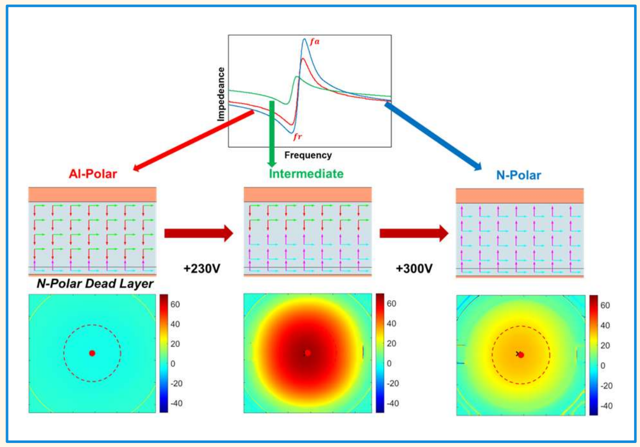

***Index Terms*— Piezoelectric transducers, ferroelectric devices, piezoelectric polarization, PMUT, ScAlN, ultrasound, microelectromechanical systems.**

I. Introduction

Ferroelectricity is an extension of the piezoelectric properties of materials, allowing for the remanent polarization of piezoelectric materials to be altered in magnitude and direction by an external electric field yet additionally retain this polarization after the field is removed. This is in contrast to non-ferroelectric piezoelectric materials, which do not retain the change to their remanent polarization after the external field is removed and revert to their original behaviour. Different polarization domain configurations will alter the film's elastic and piezoelectric properties, allowing for reconfigurable or

This research was supported by A*STAR under "Piezo Specialty Lab-in-Fab 2.0" (Grant No. I2301E0027).

Sean Jun Zhong Wong is currently a PhD student at the National University of Singapore, Singapore 119077, and a scholar under the Agency for Science, Technology and Research, Singapore (e-mail: stu-wjzs@a.star.edu.sg).

Chen Liu and Yan Hong are with the Institute of Microelectronics, Agency for Science, Technology, and Research, Singapore (e-mail: liuc@a-star.edu.sg, hong_yan@a-star.edu.sg).

Chengkuo Lee is with the National University of Singapore, Singapore 119077 (email: elelc@nus.edu.sg).

Alessandro Stuart Savoia and Muhammad Usman Khan are with the Department of Industrial, Electronic, and Mechanical Engineering, Roma Tre University, 00146 Rome, Italy (e-mail: alessandro.savoia@uniroma3.it, muhammadusman.khan@uniroma3.it).

Yao Zhu is with the Institute of Microelectronics, Agency for Science, Technology, and Research, Singapore (e-mail: zhuya@a-star.edu.sg).

This article has been accepted for publication in IEEE Transactions on Ultrasonics. This is the author's version which has not been fully edited and content may change prior to final publication. Citation information: DOI 10.1109/TUSON.2026.3722028

Highlights

- **The change in piezoelectric figures of merit of 30% ScAlN as the ferroelectric polarization varies is catalogued in this paper, with the existence, location, and impact of a ferroelectric dead layer within the film explored.**
- **Piezoelectric properties are strongest at the polarization saturation points in either Al-polar or N-polar directions, with N-polar being slightly favoured due to the asymmetry of the dead layer.**
- **These findings allow for improved characterization and estimation of the ferroelectric polarization of ScAlN and its effects on piezoelectric, frequency, and mechanical properties in the film.**

tuneable MEMS devices, which is especially promising for in-sensor computing.

In the field of MEMS devices, micromachined ultrasonic transducers (MUTs) are a growing and potentially pivotal innovation especially for the biomedical industry, particularly due to their small form factor, low power consumption, and their applicability in portable and flexible applications [1], [2], [3]. Numerous potential applications have been identified for MUTs, including but not limited to biomedical imaging [4], [5], [6], [7], [8], [9], ultrasound therapy [10], [11], drug delivery [12], [13], wireless powering of implantable biomedical devices [14], [15], industrial range-finding [16], [17], [18], [19], and reconfigurable or otherwise tuneable ultrasonic devices [20], [21], [22], [23]. Two key designs have forked from the MUT concept: capacitive MUTs (CMUTs) that utilize the capacitance between two electrodes separated by a micron-scale gap, and piezoelectric MUTs (PMUTs) that utilize an active piezoelectric layer between the two electrodes. For PMUTs, the piezoelectric properties of the active layer are of utmost importance, thus a majority of previous research has focused on the use of lead zirconate titanate (PZT) due to its high piezoelectric constant $e_{31,f}^2$ [1], [24], [25], [26], [27], [28], [29]. However, although PZT is additionally a ferroelectric material, it is unsuitable for further exploration of spontaneous polarization within PMUT devices due to its low coercive field, rendering it unable to maintain a switched polarization during device operation [30], [31].

ScAlN, an introduction of scandium into the commonly-seen piezoelectric material AlN, is a promising and upcoming piezoelectric material that shows practical and applicable ferroelectric properties once the scandium doping concentration crosses 27% [32]. While AlN is touted as having good qualities for sensing devices in particular due to its low dielectric constant ε_{33}, it performs poorly as a transmitter due to the low piezoelectric constant $e_{31,f}^2$ [1], [26], [33]. With the introduction of scandium doping, the transmissive properties of AlN are improved with only a relatively minimal decrease to the receiving properties, while also inheriting AlN's lead-free material composition and temperature compatibility with typical CMOS processes [34]. This has resulted in a sharp increase in the use of ScAlN in recent years for PMUT design, especially in applications where both the transmissive and receiving qualities are essential [35], [36], [37], [38].

In this paper, 30% scandium-doped aluminium nitride

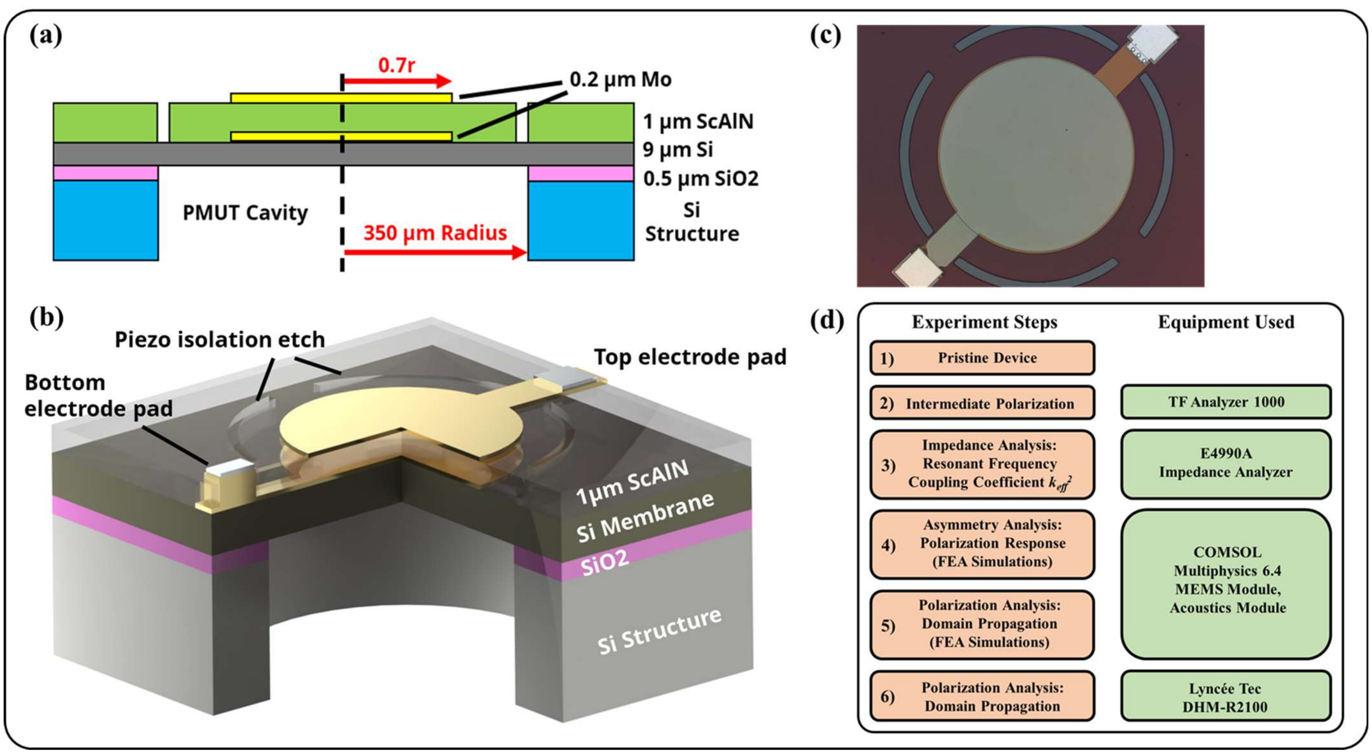

Fig. 1. **(a)** Cross-sectional PMUT device schematic; **(b)** Isometric 3D render of PMUT device, showing electrode connections and piezoelectric isolation trenches; **(c)** Top-down optical image of PMUT device taken with laser doppler vibrometer; **(d)** Experiment steps shown in this paper as well as the primary equipment or program used for each step.

This article has been accepted for publication in IEEE Transactions on Ultrasonics. This is the author's version which has not been fully edited and
content may change prior to final publication. Citation information: DOI 10.1109/TUSON.2026.3722028

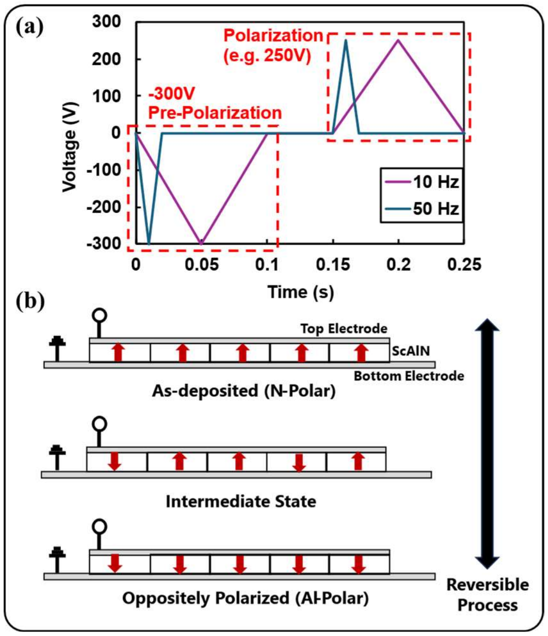

Fig. 2. **(a)** Example V-t plot showing the triangular pre-polarization pulse and polarization pulse applied for 10 Hz and 50 Hz polarization signals. The pre-polarization pulse is always kept at a magnitude of 300 V and with an opposite sign from the polarization pulse, which ranges between 200 and 300 V; **(b)** Conceptual diagram of domain polarization showing the as-deposited N-polar state and the oppositely polarized Al-polar states of the PMUT device, as well as the intermediate state with varying degrees of positively and negatively polarized domains.

($Sc_{0.3}Al_{0.7}N$) is used as the active piezoelectric material due to its higher coercive field requirement compared to PZT, allowing for intermediate polarization states to form and be maintained during device operation. ScAlN has been explored as a promising ferroelectric material as early as 2019 [32], [39]. Since then, various device designs utilizing unique properties of ferroelectricity have been showcased by research groups, typically using lead zirconate titanate (PZT) or scandium-doped aluminium nitride (ScAlN) as their active materials [40], [41], [42], [43], [44], [45]. Although research has been done towards evaluation of the piezoelectric metrics after polarization switching in ScAlN [46] and the clamping effect on such switching mechanisms [47], a numerical analysis of the ferroelectricity on both material and device parameters has not yet been catalogued especially for the intermediate polarization states between the saturated end states. This paper aims to plug this current research gap and provide device-specific research in ferroelectric materials for use in reconfigurable or tuneable MEMS devices. Briefly, this paper covers the methodology for the ferroelectric polarization of a PMUT device to achieve intermediate state poling, measurements and analysis of the effects of the intermediate states, an exploration of the asymmetrical response, and a comprehensive study into the static deformation and domain propagation of the device in its intermediate states.

II. Materials and Methods

As a test vehicle for the ferroelectrically-polarized intermediate states of 30% ScAlN, a 350 μm cavity radius PMUT structure with the piezoelectrically-active stack schematic shown in Fig. 1(a) is used. This unimorph PMUT stack consists of a 720 μm silicon structural layer, 0.5 μm SiO_2 layer, 9 μm silicon membrane layer, 0.2 μm molybdenum bottom electrode, 1 μm $Sc_{0.3}Al_{0.7}N$ piezoelectric active layer, and a 0.2 μm molybdenum top electrode. Both electrodes are deposited with a coverage of 70% of the cavity radius (245 μm). The PMUT is further covered with a 0.2 μm oxide passivation layer (not shown). A 3D render and optical image of the PMUT structure are shown in Fig. 1(b) and Fig. 1(c) respectively. Fig. 1(d) shows, in chronological order, a snapshot of the various experiments conducted in this paper as well as the most significant piece of equipment utilized in each experiment.

A. Polarization Switching

The as-deposited polarization direction of the ScAlN layer is in the N-polar direction. For consistency we label this direction as the positively-polarized direction and is equivalent to an upward-facing polarization. In order to perform polarization

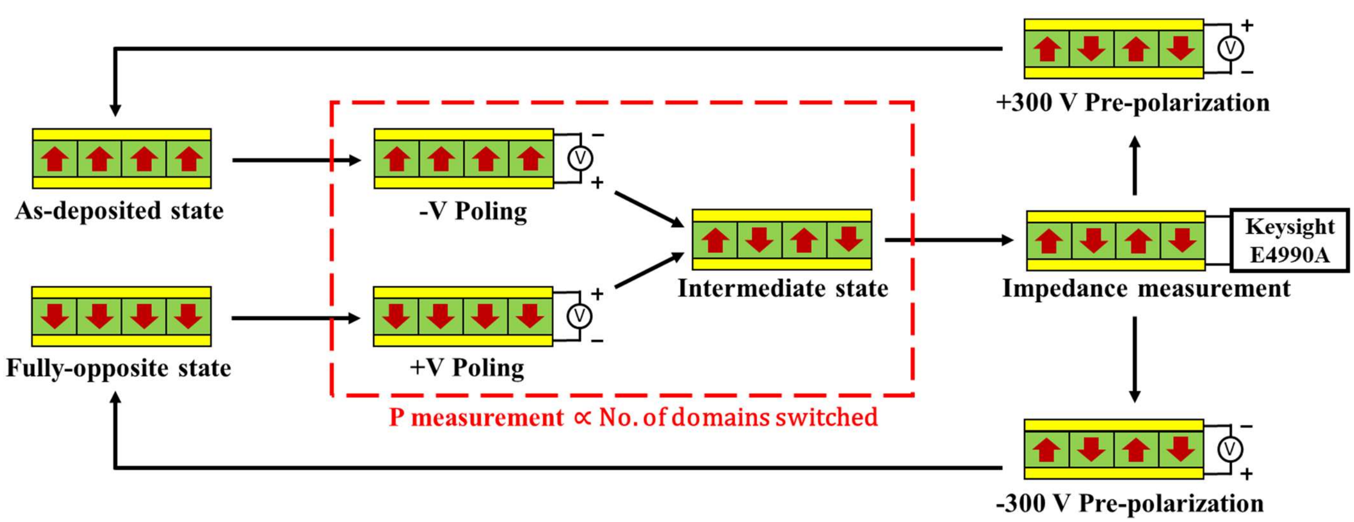

Fig. 3. Flow of experimental steps for device polarization, starting from a PMUT device in its as-deposited state and ending with an impedance measurement of the partially-switched device. Before each measurement, a 300 V magnitude pre-polarization pulse returns the device to a fully polarized state (either as-deposited N-polar or oppositely switched Al-polar). The polarization measurement is performed simultaneously with the intermediate poling process.

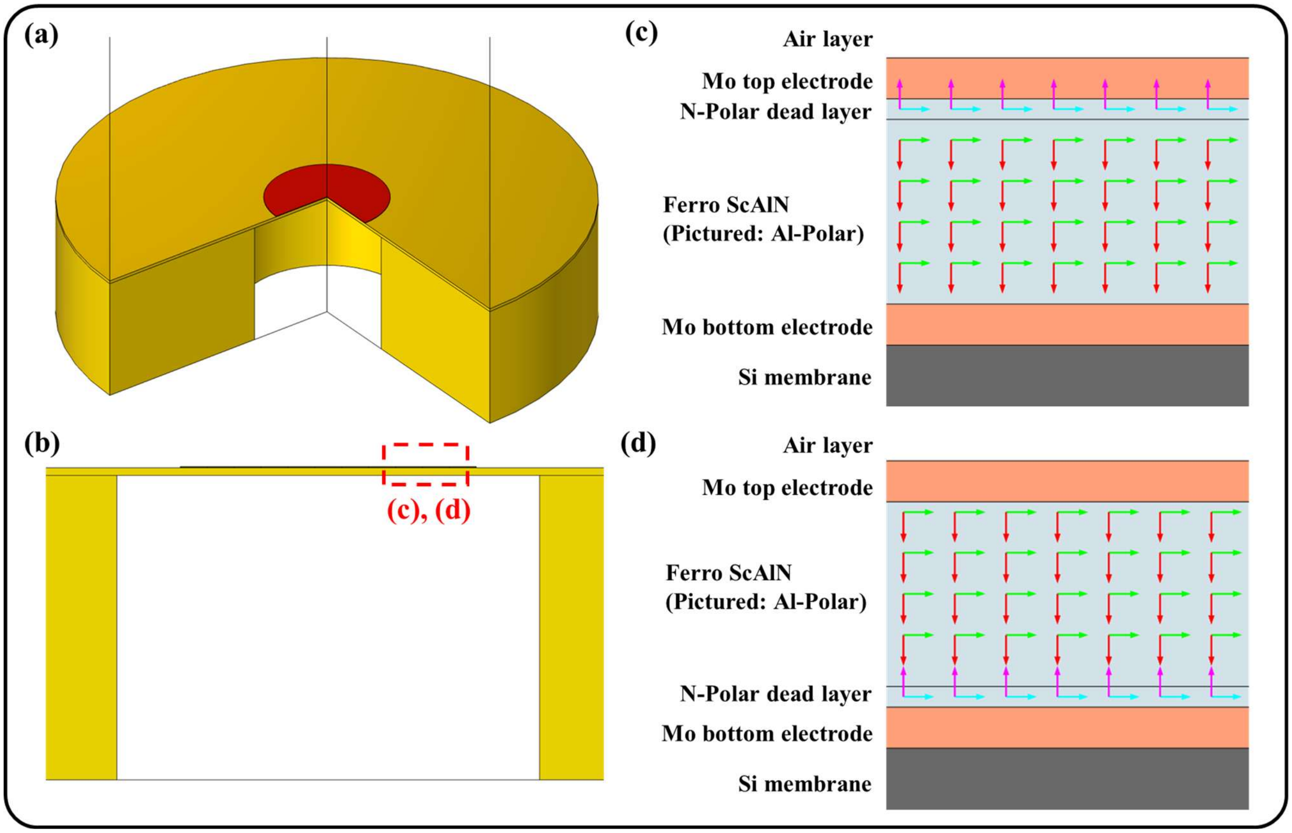

Fig. 4. Simulated COMSOL Multiphysics FEA models of **(a)** 2D axisymmetric PMUT model for row-based domain simulation; **(b)** 2D rectangular PMUT model for column-based domain simulation with cross section showing ferroelectric dead layer with coordinate systems for polarization simulation for: **(c)** top electrode interface dead layer and **(d)** bottom electrode interface dead layer. In both cases, the dead layer is an unswitchable domain with an as-deposited positively polarized (N-polar) direction represented by the upward-facing coordinate system. Each domain within the ferroelectric ScAlN layer can be switched between the downward-facing negatively polarized (Al-polar) direction and the N-polar direction.

switching of the ScAlN film, a pulse sequence as shown in Fig. 2(a) consisting of a two monopolar triangular waves, i.e., a pre-polarization pulse and a polarization pulse, is applied over the Mo electrodes with the top electrode as the terminal. Both the pre-polarization and polarization pulses, each consisting of a series of 201 voltage points at equally distributed intervals, are applied over a period of 100 ms (10 Hz, 0.25 ms interval) or 20 ms (50 Hz, 0.05 ms interval) using a TF Analyzer 1000 ferroelectric test system (aixACCT, Aachen, Germany). Each pulse is evenly split in the temporal domain between a rising component and a falling component with each component consisting of 100 points (for a total of 402 points for the entire cycle).

In prior literature, it is noted that the mean coercive field $(E_C^{+}-E_C^{-})/2$ is dependent on the residual stress T_r [32], [40] and therefore this work determines the mean coercive field for the PMUT devices experimentally, where it is found to be within 2.55 – 2.65 MV/cm (255 – 265 V) range. Thus, to ensure the resulting electric field is greater than the coercive field and so the device is fully reset to the opposite direction, the pre-polarization pulse is kept at a magnitude of 300 V (E = 3 MV/cm) with a direction that is opposite that of the subsequent polarization pulse, which has a magnitude between 225 and 300 V. This pre-polarization pulse with the same pulse duration ensures that all domains have been reset to the opposite polarization before each polarization measurement. During the poling process, the polarization measurement in μC/cm^2 over the range of voltages is collected by the ferroelectric test system. Fig. 2(b) shows a conceptual diagram of the domain polarization within the film between the N-polar direction and oppositely-polarized Al-polar directions. The impedance of the polarized device over a frequency sweep of ±20 kHz close to the resonant is measured with an E4990A impedance analyzer (Keysight Technologies, Santa Rosa, CA, USA) within a short duration (~1 minute) of the poling process, and the resonant and anti-resonant frequencies are extracted. The piezoelectric coupling coefficient k_{eff}^2 for each intermediate state polarization is calculated using equation (1), where f_r is the resonant frequency of the device and f_a is the anti-resonant frequency.

$$k_{eff}^2 = \frac{fa^2 - f\ ^2}{fa^2} \quad (1)$$

The overall flow for the polarization switching experiment, inclusive of remanent polarization and impedance measurements, is presented in Fig. 3. Although the impedance measurements were performed within a short period after poling, the devices were allowed to rest for 2 hours before being subsequently re-examined and it was found that there were no short-term relaxation effects.

B. Finite Element Analysis

The COMSOL Multiphysics 6.4 program, with active MEMS module, was used for Finite Element Analysis (FEA)

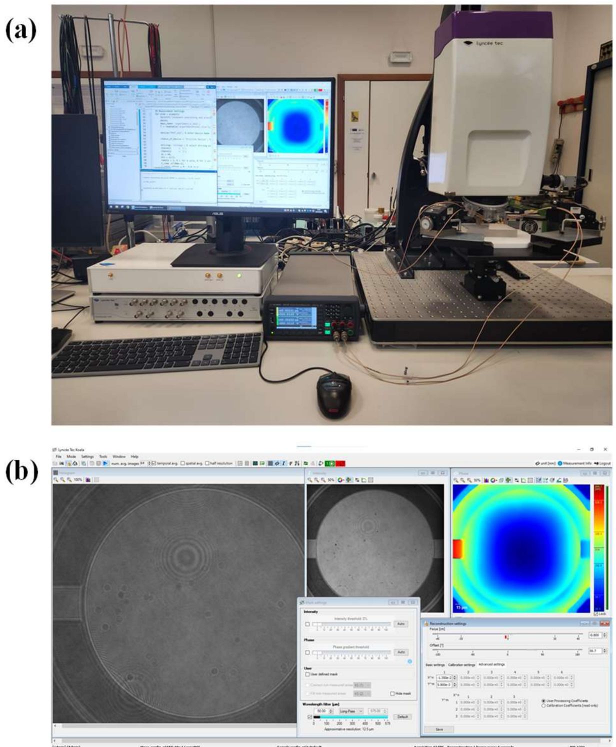

Fig. 5. **(a)** Experimental setup for mode shape analysis utilizing digital holographic microscope and source/measure unit **(b)** Configuration setup for digital holographic microscope operation with live hologram, intensity, and phase reconstruction.

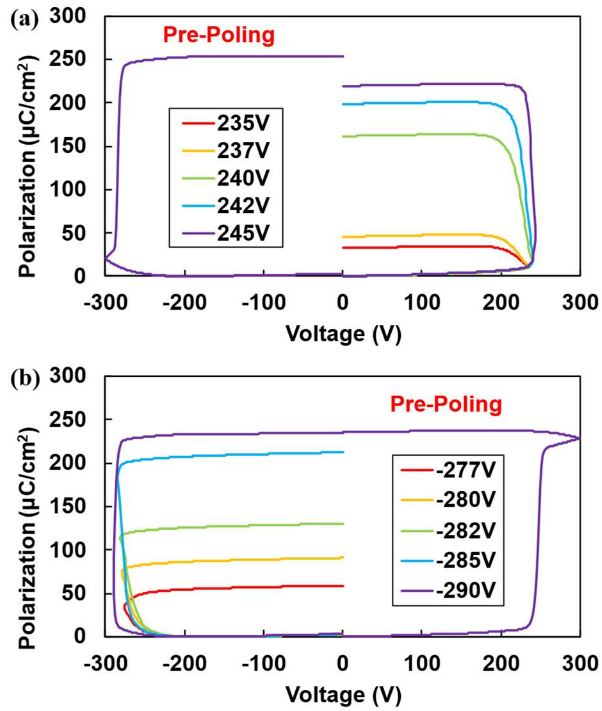

Fig. 6. Ferroelectric P-V hysteresis loops for: **(a)** 50 Hz positive polarity and **(b)** 50 Hz negative polarity. The single half-loop shows the 300/-300 V pre-poling voltage applied to the film prior to each applied poling voltage. This ensures that all domains have been switched to the opposite direction before poling.

simulations of the PMUT design and domain polarization analysis. Two models were prepared for this simulation as shown in Fig. 4(a) and (b): a 2D axisymmetric model for an axially propagating (thickness-wise along the ScAlN layer) domain structure about the central PMUT axis and a 2D plane-strain model for a laterally propagating (radius-wise along the ScAlN layer) domain structure through the PMUT radius. The difference in model is chosen as the lateral propagation in an axisymmetric model would simulate a ring-shaped domain propagation within the film rather than a rectangular block propagation. Both models include an acoustically modelled air interface within the PMUT cavity as well as above the PMUT structure, with corresponding acousto-mechanical interface.

In order to investigate the likely thickness and position of the dead layer within the thin-film, we consider the experimental data of five of the PMUT devices. The ratio of the polarization magnitudes between the opposite polarization saturation points is calculated for each device, as well as the ratio of the coupling coefficients between those same points. The polarization ratio is used to estimate the range of thicknesses for the dead layer under the assumption that the final polarization represents an estimation of the percentage of domains switched towards the corresponding direction. To further narrow down the position of the dead layer within the film, the ratio of the coupling coefficient k_{eff}^2 between the same opposite saturation points is additionally considered. The minimum and maximum of both ratios creates a bounded region that represents the most likely area for the thickness of the dead layer. Simulation data for different various dead layer thicknesses on either the top or the bottom of the film is additionally plotted to estimate the position of the dead layer in the film. For further verification of the dead layer position and thickness, we perform a comprehensive FEA simulation using two combinations based on the experimentally-obtained k_{eff}^2 data: a 0.1 μm dead layer at the interface between the bottom electrode and the ScAlN layer (of which 0.9 μm remains switchable) and a 0.05 μm dead layer at the interface between the top electrode and the ScAlN layer (of which 0.95 μm remains switchable). The coupling coefficient k_{eff}^2 is obtained from the simulation data of the impedance curves for different percentages of polarized domains.

Fig. 4(c) and (d) describes the simulated ferroelectric dead layer in COMSOL, displaying the rotated reference coordinate system used for the upward-facing (N-polar) and downward facing (Al-polar) ScAlN layers. Using this coordinate system mimics the ferroelectric polarization change present in the experimental device on a per-domain basis. The 0.1 μm dead layer utilizes the N-polar direction coordinate system while the remaining domains of the ScAlN layer are changed between the two polarization directions to represent the intermediate polarization states. The operational voltage is kept at 1 V peak-to-peak for the frequency analysis.

For the FEA simulations intended to showcase the static deformation, the voltage is kept at a static 40 V DC for both the lateral and axial domain polarization propagation directions. For the laterally propagating polarization, the rectangular 2D model is used and shows the asymmetrical static deformations as the Al-polarized domains grow from the as-deposited N-polar to the switched Al-polar state, and the shift in asymmetry as 46% of switchable domains in Al-polar state shift from the leftmost region to the centre region. For the axially propagating polarization, the 2D axisymmetric model is used and shows the

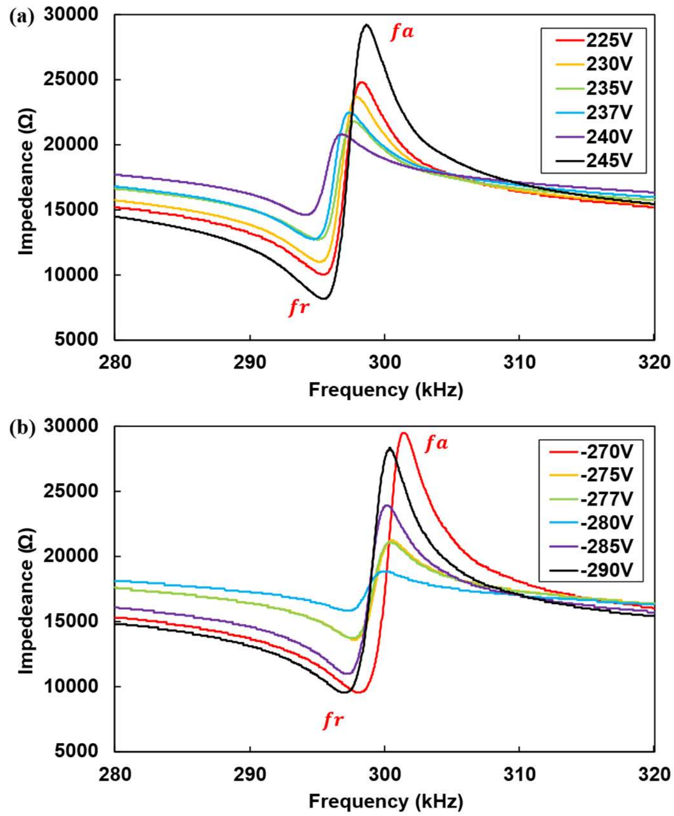

Fig. 7. Device impedance magnitude response versus frequency plots for: **(a)** 50Hz positive polarity; **(b)** 50Hz negative polarity. The shift in resonant frequency fr (minimum point of the impedance plot) of the device can be seen across various poling voltages. The coupling coefficient k_{eff}^2 can be calculated from the observed fr and fa with equation (1).

symmetrical static deformations with corresponding change in the deformation magnitude and direction (in this case, for a film without internal stresses from fabrication) as the film becomes increasingly Al-polar in, and the corresponding change in deformation magnitude as 40% of switchable domains in Al-polar state shift from the bottommost region to the topmost region.

C. Static Deformation Profile Analysis

To analyse the change in static deformation profile of the polarized PMUT devices, a digital holographic microscope (DHM) DHM-R2100 (Lyncée Tec SA, Lausanne, Switzerland) with attached laser pulsed stroboscopic unit is utilized with the setup shown in Fig. 5(a). The PMUT devices are polarized utilizing a source/measure unit (SMU) B2912B (Keysight Technologies, Santa Rosa, CA, USA), which is additionally used to supply a 40 V DC bias to generate a static deformation in the PMUT device. The DHM is first calibrated for the unbiased device measurement utilizing the first optical wavelength (λ = 684.984 nm) with a wavelength long-pass filter of 50 µm and 64-sample temporal averaging. A screenshot of the configuration setup for the DHM Koala Stroboscopic V5 operational program (Lyncée Tec SA, Lausanne, Switzerland) is shown in Fig. 5(b) and includes the hologram, intensity, and phase live reconstructions of the PMUT device as well as the mask and digital tilt configuration.

The SMU provides two independent channels, each capable of generating up to ±210 V. The devices under test were driven differentially by connecting the two channels to opposite terminals of the PMUT and driving them simultaneously with equal amplitude and opposite polarity (±150 V short pulses per channel). This resulted in a differential voltage of up to ±300 V across the load while keeping each channel within its voltage limit.

A bipolar triangular pulse of ±300 V with a duration of 200 ms was applied using the SMU as a pre-polarization pulse to reset the PMUT device prior to each dataset, and a reference phase profile was acquired using the DHM. The bipolar triangular pulse was generated with the SMU operated in list mode, using discrete voltage steps of 20 µs duration each. As an initialization procedure, 1250 steps were used to ramp up the voltage from 0 to +300 V, with additional 1250 steps to return from +300 V to 0 V. This was followed by 5000 0 V steps (corresponding to 50 ms), after which 1250 steps were used to ramp down from 0 to –300 V, and another 1250 steps to return from –300 V to 0 V, completing the initialization.

For each acquisition, a monopolar triangular pulse of fixed 300 V magnitude, followed by a monopolar triangular pulse of opposite direction and varying voltage (200 V – 300 V) is applied and respective height profile is acquired. A DC bias voltage of 40 V was then applied, and the resulting biased height profile is obtained. The voltage is varied between each acquisition by 1 V increments from 200 V to 300 V, after which the acquisition is repeated with an identical pre-polarization pulse and opposite potentials. As it was previously noted that the PMUT devices suffered no noticeable relaxation effects within a timeframe of 2 hours, the DHM measurements were acquired within 2 hours of the poling process being performed.

Post-processing of the acquired data was performed in MATLAB R2022a. To ensure more accurate visualization, a tilt and planar correction was applied to all height map data obtained from the acquisition, with the four corner points acting as the zero reference. Additionally, height difference data maps are obtained by direct subtraction of height maps from each other post-correction, in order to account for the effects of the intrinsic membrane curvature in the measurement.

III. Results

A. Intermediate Polarization States

We achieve the intermediate polarization states at voltages between 230 V and 245 V (2.3 to 2.45 MV/cm) for N-polar and -260 V to -290 V (-2.6 to -2.9 MV/cm) for Al-polar using a 50 Hz (10 ms triangular pulse duration) polarization pulse. At voltages between -260 V and 230 V, there is little change in the domain polarization, and it is considered to be below the film coercive voltage. At voltages above 245 V or below -290 V, the film has reached the polarization saturation point and there is little change in the remanent polarization.

The pre-poling process at 300 V (3 MV/cm) magnitude with the same pulse duration ensures that all domains have been reset to the opposite polarization before each polarization measurement. Subsequently, the applied poling voltage results in the switching of a number of domains towards the desired polarity. Intermediate polarization states are distinguished by

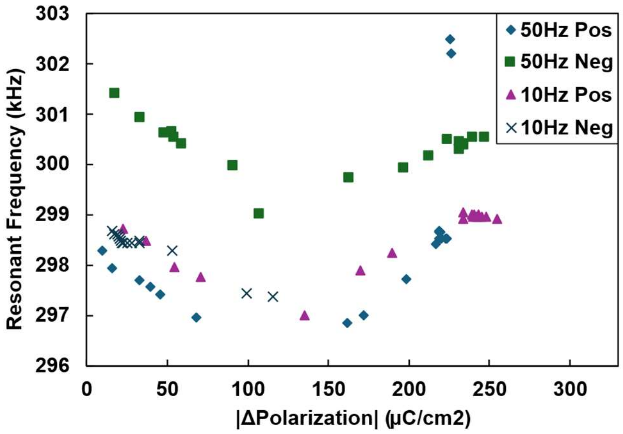

Fig. 8. Change in device resonant frequency with polarization at various poling voltages and frequencies. There is a visible dip in resonant frequency near the neutral intermediate polarization point of 100-150 μC/cm^2.

the final remanent polarizations as shown in Fig. 6, which increases up to a maximum polarization at the saturated state.

It is notable that the required coercive voltage magnitude for the negative (Al-polar) polarization switching is higher than in the positive (N-polar) direction. However, the final remanent polarization at the saturation point is likewise higher in the negative direction than in the positive direction, with a final saturated remanent polarization of 269.8 μC/cm^2 towards the negative direction compared to 254.7 μC/cm^2 towards the positive direction. The greater polarization magnitude indicates that, at the coercive voltages, a greater volume of domains are switched towards the Al-polar direction in the film. In both cases, the measured remanent polarization for the 30% ScAlN film is slightly greater than the ~200 μC/cm^2 from *Fichtner et al.* and noticeably larger than the approximate spontaneous polarization constant of AlN of 126 μC/cm^2 [32].

B. Effect of Intermediate Polarization on Film Performance

The impedance spectra in Fig. 7 showcase the shift in the gathered resonant and anti-resonant frequencies as the poling voltages approach the saturation point. At low voltage magnitudes (pre-coercive voltage), there is limited domain switching in the ScAlN film and thus the impedance spectrum is similar to at the saturation point. At higher poling voltages approaching polarization saturation, there is a visibly larger difference in the resonant and anti-resonant frequencies with correspondingly higher coupling coefficient k_{eff}^2.

There is a shift in resonant frequency as the thin-film polarization reaches the neutral state (equal domain volume polarized in either direction) as shown in Fig. 8, dropping by as much as 2.4 kHz at the lowest point for the 50 Hz negative poling in comparison to the pre-poled state, a decrease of 0.8%, while it can be seen that the positive (N-polar) poling states have a higher average resonant frequency of about 0.2-0.3%. The resonant frequency subsequently increases back to the original value as the polarization approaches saturation, indicating that the neutral state represents a global minimum in the resonant frequency of the device. The reduction in resonant frequency at the intermediate polarization states is most likely caused by the relaxation of internal stresses, brought about by the lowered inter-boundary stresses from the mixed Al and N-polar domains. In Section III.D, the membrane curvature is estimated from the unbiased DHM profiles and used as a

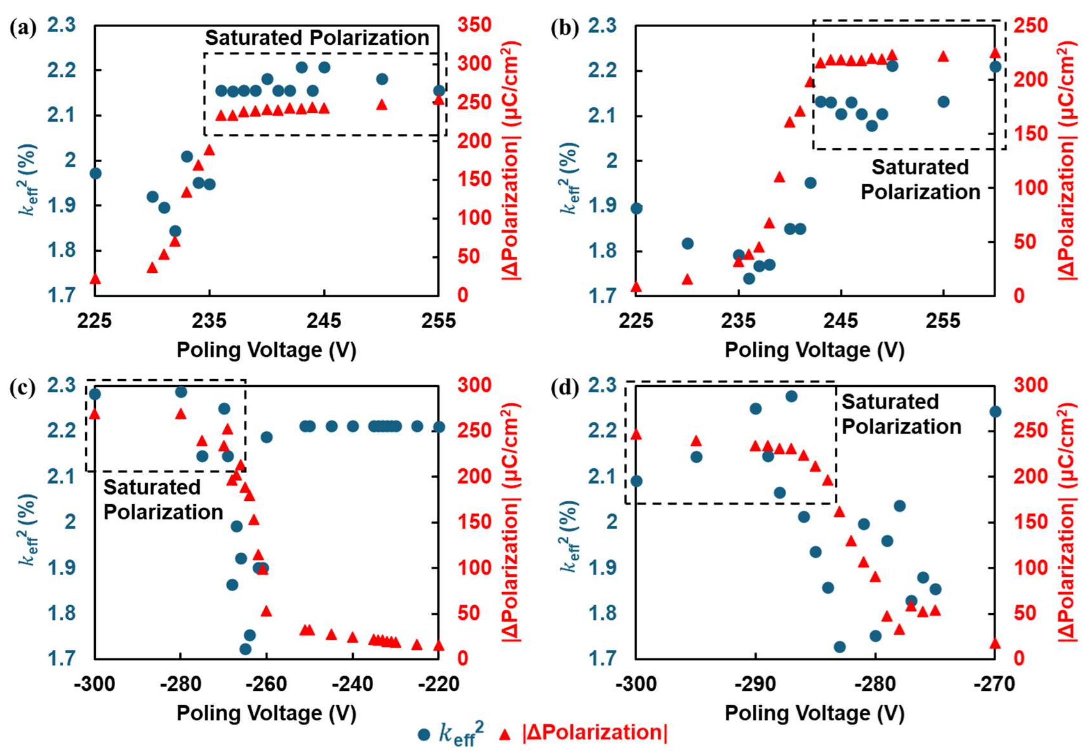

Fig. 9. Poling voltage effect on coupling coefficient k_{eff}^2 and change in polarization for: **(a)** 10 Hz positive polarity (Al-polar to N-polar); **(b)** 50 Hz positive polarity (Al-polar to N-polar); **(c)** 10 Hz negative polarity (N-polar to Al-polar); **(d)** 50 Hz negative polarity (N-polar to Al-polar). Intermediate polarization states can be seen as the region where the change in polarization with voltage is the steepest. Saturation states for each polarity and frequency are clearly noted as regions where polarization does not increase with voltage.

This article has been accepted for publication in IEEE Transactions on Ultrasonics. This is the author's version which has not been fully edited and content may change prior to final publication. Citation information: DOI 10.1109/TUSON.2026.3722028

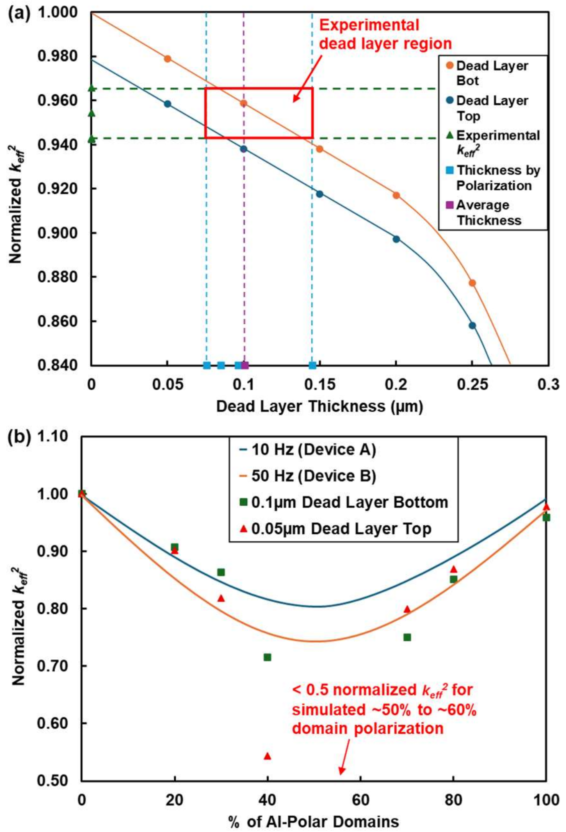

Fig. 10. **(a)** Polarization ratio between Al-polar and N-polar saturation points of experimental devices compared to the normalized coupling coefficient of experimental data at Al-polar saturation. The coupling coefficient ratio between Al- and N-polar saturation points is shown for top and bottom dead layers with varying thicknesses, with the region bounded by the four dotted lines most likely to contain the true dead layer thickness. **(b)** Change in normalized coupling coefficient k_{eff}^2 with percentage of Al-polarized domains in thin film. Simulated FEA data for top and bottom dead layers - with thicknesses matching the horizontal region in (a) - are shown alongside the 10 Hz and 50 Hz experimental data from two devices, with the 0.1μm dead layer on the bottom of the film having the best match to the experimental data.

device-level indicator of polarization-dependent changes in the effective mechanical stress/strain state of the PMUT membrane.

The plots in Fig. 9 (a) – (d) show the change in coupling coefficient k_{eff}^2 with the device remanent polarization for 10 Hz and 50 Hz polarization pulses. At the coercive voltages E_C where the remanent polarization begins to rise sharply (230 V and -260 V for 10 Hz polarization pulse, 235 V and -280 V for 50 Hz polarization pulse), experimental data shows a similar increase in k_{eff}^2, plateauing at the saturated polarization regions. Beyond the voltages near the beginning of the saturated regions, there is little observable increase in polarization or k_{eff}^2. It is notable that k_{eff}^2 is, on average, higher when positively polarized by approximately 0.1%, indicating a performance favourability towards the N-polar direction in the film. The k_{eff}^2 in the N-polar direction is significantly more stable than in the Al-polar direction, suggesting that the domain structure in the N-polar direction retains a similar propagation pattern each cycle. In addition, the coercive voltage E_c is significantly higher in the negative direction, indicating a level of domain pinning which imposes a greater 'inertia' to the polarization in the Al-polar direction.

The V-shaped k_{eff}^2 response is consistent with partial cancellation of the oppositely signed piezoelectric contributions of coexisting N-polar and Al-polar regions. When both orientations coexist in comparable fractions, the net modal electromechanical response is reduced. As either orientation becomes dominant, k_{eff}^2 increases toward saturation. The asymmetry between the saturation endpoints is quantified by the measured Al-polar/N-polar k_{eff}^2 ratios of 0.943-0.966 across five devices and is consistent with the effective N-polar unswitchable interfacial fraction considered in Section III.C. As k_{eff}^2 is an effective device parameter, the present measurements do not independently separate the intrinsic piezoelectric, dielectric, stress, and geometric contributions.

C. Dead Layer Exploration and Verification

As noted, the asymmetry in the device performance metrics at the saturated polarizations signifies a skewed performance favouring the positive (N-polar) polarization direction. This is likely caused by the existence of a piezoelectric dead layer that is practically non-ferroelectric (i.e. it cannot be switched at the same coercive voltage as the rest of the film) and is thus fixed in the as-deposited N-polar direction. Due to the piezoelectricity that is still present in this layer, the performance of the film in the N-polar direction is enhanced, while the performance in the Al-polar direction is diminished. Previous material-level studies of polarized ferroelectric ScAlN films have investigated polarization propagation at the material and domain scales [48], [49] and have reported dead layers or unswitchable interfacial regions associated with nitrogen-related defects and interfacial strain [50], [51], [52], [53]. Thickness-dependent switching asymmetry and interfacial effects have also been observed in very thin (∼50 nm) 37% ScAlN films [54]. These studies provide prior physical precedent for consideration of a ferroelectrically dead layer when interpreting the asymmetric response of ScAlN thin-film devices. Although they do not characterize the Mo/$Sc_{0.3}Al_{0.7}N$/Mo film investigated in this work, the works provide evidence towards the dead layers being located at the interface between the ScAlN layer and other interfaces. Therefore, in this work, we attribute the asymmetrical response of the film to the un-switchability of a dead layer and investigate the most likely positioning and thicknesses. The asymmetry between the N-polar and Al-polar saturation states is evaluated using a device model containing a fixed N-polar dead layer. The following sections present a device-level evaluation of its effective thickness, likely interfacial position, and influence on PMUT performance. The resulting thickness and location should therefore be interpreted as model-based estimates rather than direct structural measurements. The referenced published material studies are used as physical context for the effective device model and not as a substitute for characterization of the present film.

Fig. 10(a) showcases the results of the calculated ratios of the polarization (vertical dashed lines) and the k_{eff}^2 (horizontal dashed lines) of the five chosen devices. For the range of devices, the ratio of k_{eff}^2 is between 0.943 and 0.966, as represented by the horizontal dashed lines. The average polarization ratio of 0.8992 corresponds, under the assumptions of the adopted model, to an effective unswitchable fraction of 10.08% of the ScAlN thickness, equivalent to 0.1008 μm. It should be additionally noted that the extrapolated trend for the bottom layer data crosses the x-axis origin at a normalized k_{eff}^2 of 1.0, which is the expected intersection point if there is no dead layer present in the film. The results shown in Fig. 10(b) show the two simulation points bounded by the horizontal dashed lines in Fig. 10(a), alongside the 10 Hz and 50 Hz experimental data for two separate devices. Among the configurations investigated, the bottom-interface model provides the closest agreement with the measured polarization and k_{eff}^2 ratios. The experimental results therefore support a bottom-weighted effective N-polar unswitchable fraction within the model of approximate 10% thickness of the piezoelectric layer, but does not establish its exact physical thickness, microscopic structure, composition, or interface location. In general, the simulated data for the 0.1 µm bottom-interface dead layer shows the best fit with the current experimental data with a higher asymmetry towards the negative (less Al-polar domains) region as compared to the 0.05 µm top-interface dead layer.

In previous literature, it has been suggested that the increased compressive strains near the boundary between wurtzite ScAlN and GaN produce a twofold effect of increasing the ferroelectric coercive fields required for polarization switching and additionally promote generation of N-type vacancies within the material, which contributes to degraded dielectric performance [55]. As a result, the reversibility of the polarity at this interface region is heavily degraded and a dead layer is formed. Although the interface material in this PMUT device is a Mo electrode rather than a GaN semiconductor layer, the increased compressive stress at the bottom thin-film interface is likely to produce a similar effect in the ScAlN film. As the scandium concentration used in this paper (30%) is only slightly higher than the earlier noted minimum concentration for practical ferroelectricity (27%), even this effect could increase the coercive field requirements and degrade dielectric performance enough for a substantial dead layer formation.

D. Propagation of Domain Polarization

With the thickness and position of the non-ferroelectric dead layer, an understanding of the propagation of domain polarization for the thin-film intermediate polarization states is relevant as part of the mechanism for polarization. This is a key factor in the future ability to predict the piezoelectric response of the thin-film in any state other than at either fully saturated point, as it will allow for both shape and magnitude of the static response to be more accurately estimated.

The FEA simulated static response shapes of the device are shown in Fig. 11. For the laterally propagating domains in Fig. 11(a) and (c), there is a clear shift in the asymmetry of the static response as the Al-polarized domains shift from the edge towards the centre of the film. The magnitude of the asymmetrical response is significantly more prominent with an increased number of Al-polarized domains, and the magnitude of the positive displacement increases as the Al-polarized domains are positioned closer to the centre. For the axially propagating domains in Fig. 11(b) and (d), there is no visible change in the shape of the static deflection until the Al-polar domains begin to dominate, at which point the direction of the deformation crosses the undeformed region. It is notable that in both domain propagation methods, the dead layer is a significant factor in the magnitude of the final deformation but not the shape; the fully N-polar static response is always larger in magnitude (98.9 nm vs 80.5 nm for lateral propagation and 79.5 nm vs 64.4 nm for axial propagation) than the Al-polarized static response, notably due to the N-polar dead layer providing an opposing force to the Al-polar response. The discrepancy between the fully polarized states is noted to be due to difference in the FEA models used, where the magnitude of the deformation in the planar 2D model is consistently 24 - 25% greater than the 2D axisymmetric model, and is primarily attributed to the difference in the existence of the radial boundary between the membrane and the substrate in the axisymmetric model. This variation is consistent for all simulations where the domain polarities are exactly equivalent between the two models.

Fig. 12(a) shows the height map profiles of the PMUT device after various poling pulses have been applied but without an external DC bias. Both the N-polar and Al-polar membranes are distinctly U-shaped with 23.42 nm and 77.74 nm minimum points respectively (where 0 nm referring to the points at the four corners), with the intermediate polarization state having the least curved membrane shape at 95.09 nm. Using three points along the top-electrode surface, the estimated membrane curvature is 9.59×10^{-3} mm^{-1} in the N-polar state, 7.57×10^{-3} mm^{-1} in the intermediate state, and 8.04×10^{-3} mm^{-1} in the Al-polar state. These values correspond to decreases of 21.1% and 16.2% relative to the N-polar state for the intermediate and Al-polar states, respectively.

From Fig. 12(b) which details the differences in the unbiased height maps from the as-deposited N-polar state, it can be noted that the upwards deformation increases at the intermediate states by up to 67.9 nm at the central point and is 50.2 nm higher at the Al-polar state than the N-polar state. As these states are without external DC bias, the change in membrane curvature can be purely attributed to the changes in the internal stresses of the ScAlN film, and it is clear that the film experiences the highest internal stresses at the fully N-polar state (largest U-shaped membrane with highest curvature) and the lowest internal stresses at the intermediate state (flattest membrane shape with lowest curvature). This is likely caused by the overall increase in inter-domain boundary stresses when the film domains are mostly polarized in one direction. In this case, the N-polar direction is the only direction where all domains including the dead layer are aligned; thus, the N-polar direction experiences the greatest internal stresses within the PMUT membrane. Conversely, the intermediate state experiences the largest equality between the N-polar and Al-polar domains, which leads to the least inter-domain boundary stresses and thus the most relaxed membrane shape (though it should be noted the membrane remains in a stressed U-shape regardless, simply at a lower internal stress point). The Al-polar state has a more relaxed deformation compared to the N-polar state, as the dead layer remains N-polar and thus counteracts some of the inter-domain stresses. The measured curvature trend is attributed to a polarization-state-dependent redistribution of the effective mechanical stress/strain state associated with the domain configuration. The intermediate state exhibits both the lowest estimated curvature and the minimum resonant frequency, supporting a mechanical contribution to the

This article has been accepted for publication in IEEE Transactions on Ultrasonics. This is the author's version which has not been fully edited and content may change prior to final publication. Citation information: DOI 10.1109/TUSON.2026.3722028

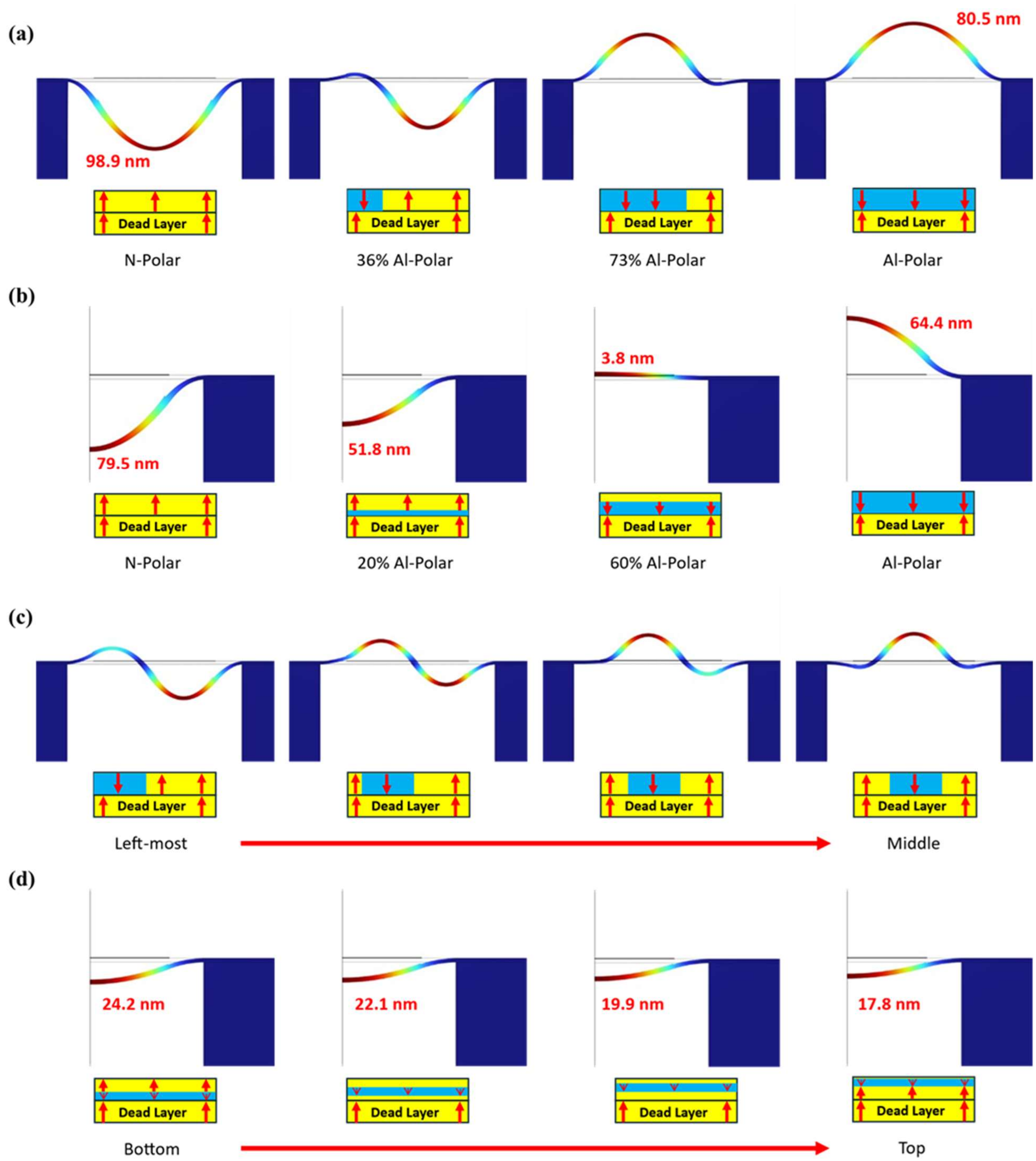

Fig. 11. FEA simulations for static deformation shape and magnitude with 40V DC bias for: **(a)** Lateral domain polarization propagation (2D model); **(b)** Axial domain propagation (2D axisymmetric model); **(c)** Asymmetry of film for 46% Al-polarized domains in lateral propagation model, from leftmost domain region to central region. This describes the asymmetrically deformed shape that would be expected to be observable should the polarization-switched domains propagate in a lateral manner; **(d)** Change in displacement magnitude for 40% Al-polarized domains in axial propagation model, from bottommost domain region to topmost region. This describes the varying displacement magnitudes of the symmetrical shape that would be expected to be observable should the polarization-switched domains propagate in an axial manner.

frequency variation. The asymmetry between the N-polar and Al-polar saturation states is consistent with the effective N-polar unswitchable interfacial fraction included in the device model. However, curvature does not uniquely determine the underlying stress distribution or separate the effects of residual stress, polarization-induced strain, trapped charge, and membrane geometry.

Additionally, we note the change in asymmetry between the various polarization states in Fig. 12(b), most specifically the intermediate states, further detailed in Fig. 12(c) showcasing the poling voltages between 230 V and 235 V with a DC bias of 40 V applied. As can be seen from the height difference maps (compared to the fully N-polar reference), there is a point in the bottom-left of the membrane (distance from centroid = 38.08 μm with angle θ = 3.882 rad) at 230 V poling voltage where the

This article has been accepted for publication in IEEE Transactions on Ultrasonics. This is the author's version which has not been fully edited and content may change prior to final publication. Citation information: DOI 10.1109/TUSON.2026.3722028

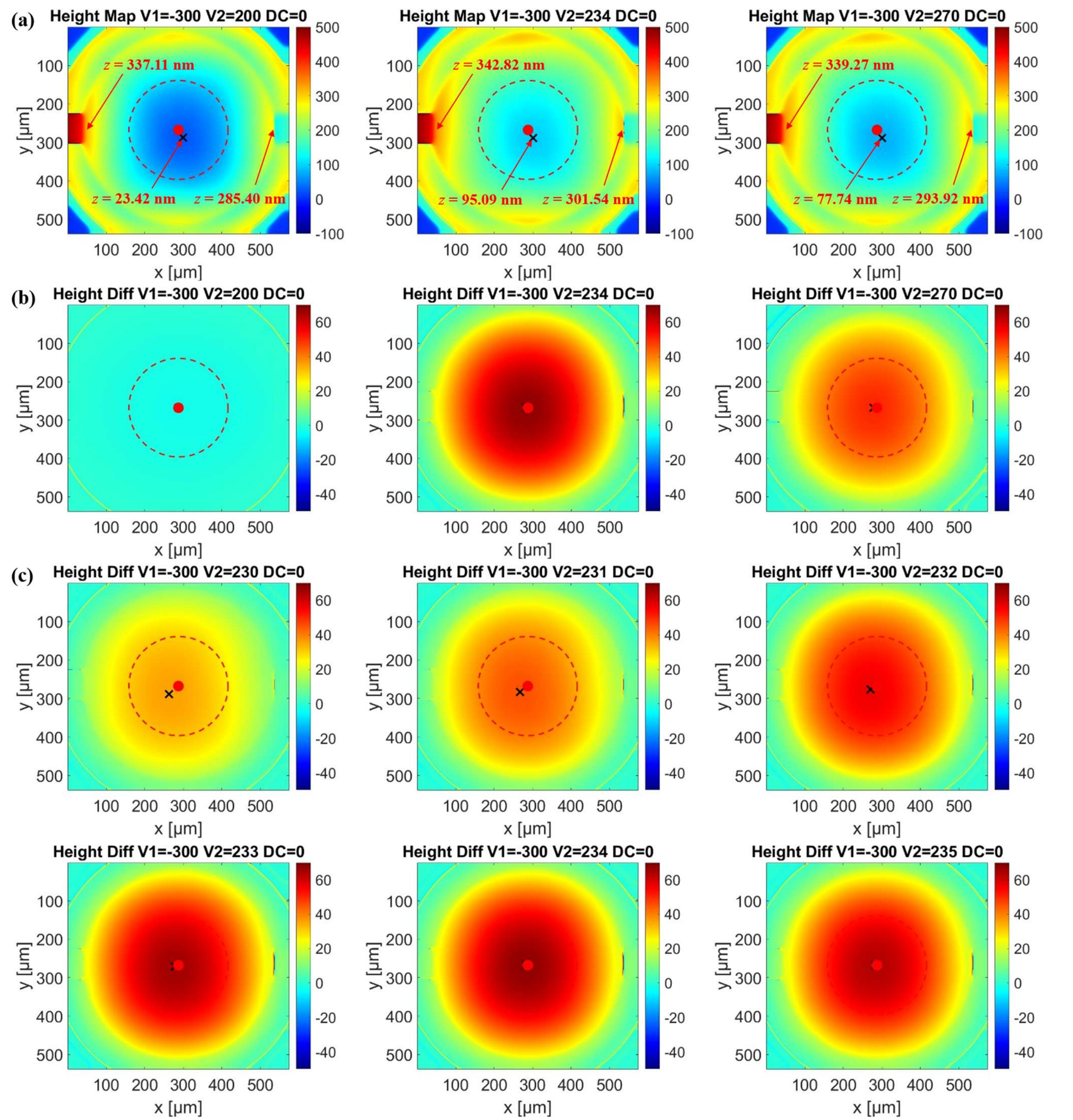

Fig. 12. DHM-collected profiles of statically deformed PMUT devices: **(a)** Height maps of the PMUT relative to the four planar corners, for N-polar (left), intermediate (middle), and Al-polar (right) states; **(b)** Height difference maps of the PMUT between the maps shown in (a) and the initial N-polar reference point; **(c)** Height difference maps of the PMUT at the intermediate states, transitioning from N-polar (V2 = 230 V) toward Al-polar (V2 > 235 V), showcasing the movement in the maximum deformation point denoted by the black X. In all figures, the yellow circular borders and dotted red circle represent the computed circular profile of the PMUT, the red dot represents the centroid point of the membrane, and the black X represents the point of maximum deformation within the membrane.

film begins to switch first, causing an asymmetrical point of deformation at the intermediate step. As poling voltage increases to 235 V, this asymmetry decreases until the minimum point overlaps with the centroid, indicating that the rest of the film 'catches up' with the polarization as voltage crosses the coercive voltage. There is thus a region of the film that may not coincide with the centroid point where the coercive voltage is lower, indicating some manner of lateral domain propagation. However, the change in deformation is relatively uniform across the membrane, especially as voltage increases, which suggests that the axial domain propagation dominates in the polarization. We thus propose that the propagation follows a hybrid model with primarily axial propagation, in a similar to the STEM analysis from previous research that shows shark-teeth shaped domains that propagate vertically through the film thickness [50]. It is further notable that the region that experiences the earlier switching occurs in a reliable location between individual polarization instances; the poling is reset between each acquisition and thus the asymmetry is systematic in nature. We also note that, upon inverting the sample and acquiring the polarization results again, the maximum deformation point is similarly inverted and thus eliminates the possibility of bias within the experimental setup.

IV. Conclusions

In summary, both Al-polar and N-polar ferroelectric polarization of a 1 μm thin-film $Sc_{0.3}Al_{0.7}N$ PMUT have been demonstrated in this paper, as well as the intermediate states between the saturated polarization endpoints. We cover the change in various performance metrics such as resonant frequency, impedance response, and coupling coefficient k_{eff}^2 over the various polarization states, and highlight the significant asymmetry of the film polarization that favours the N-polar saturation state. It is expected that, based on the improvement in k_{eff}^2, the transmitting and receiving performance at the polarized states will be the highest, with the intermediate state performance being significantly degraded. Primarily, the sensitivity of the device in both transmit and receive modes should improve proportionally with the coupling coefficient.

Among the configurations investigated, the asymmetry between the N-polar and Al-polar saturation states is best reproduced by a model containing a fixed, ferroelectrically unswitchable N-polar dead layer equivalent to approximately 10% of the ScAlN thickness (0.1 μm) at the interface with the bottom electrode. The estimated thickness and location are based on the measured polarization and k_{eff}^2 trends, along with comparison with finite-element simulations, rather than direct structural or interface characterization. The PMUT transmit and receive performance at the N-polar state (poling reinforcement of the as-deposited direction) is expected to be the highest due to the existence of this dead layer. Furthermore, the static response deformation of the thin-film PMUT is gathered in both COMSOL simulation and experimental DHM setup to explore the domain propagation over various intermediate states, demonstrating a relaxation of internal stresses at the intermediate and Al-polar states in comparison to the fully N-polar state. Additionally, the domain propagation is found to be a hybrid of lateral and axial propagation directions, however the axial directionality remains dominant within the film around the coercive voltages.

Within the PMUT domain, the results in this work present several interesting future possibilities and applications, such as performance enhancements (through reinforcement poling of the as-deposited states as well as future work targeting dead layer minimization), acoustic beam control (through poling of certain elements toward intermediate states to tune their output pressure), and thin-film internal stress adjustment (through dynamic relaxation or pre-stressing of the domain structure) for adaptive frequency driving.

Our expectation is that ScAlN will become an increasingly popular material for use in future PMUT and the derivative ferroelectric micromachined ultrasound transducer (FMUT) due to its ferroelectric switch-ability and combination of good transmit and receive properties with CMOS compatibility and lead-free composition. Future work in this area is expected, especially for in-depth crystalline analysis across the device. The intermediate states shown in this paper pave the way for tuneable PMUT and FMUT devices with between-operation or in-operation ferroelectric switching, and there is currently an unexplored research gap for future works in this field.

Acknowledgment

This research was supported by A*STAR under "Piezo Specialty Lab-in-Fab 2.0" (Grant No. I2301E0027).

References

[1] S. J. Z. Wong, K. Roy, C. Lee, and Y. Zhu, "Thin-Film Piezoelectric Micromachined Ultrasound Transducers in Biomedical Applications: A Review," *IEEE Trans. Ultrason. Ferroelectr. Freq. Control*, vol. 71, no. 6, pp. 622–637, Jun. 2024, doi: 10.1109/TUFFC.2024.3390807.

[2] E. Moisello, L. Novaresi, E. Sarkar, P. Malcovati, T. L. Costa, and E. Bonizzoni, "PMUT and CMUT Devices for Biomedical Applications: A Review," *IEEE Access*, vol. 12, pp. 18640–18657, 2024, doi: 10.1109/ACCESS.2024.3359906.

[3] Q. Ren, J. Chen, X. Liu, S. Zhang, and Y. Gu, "Design and 3D FEM Analysis of a Flexible Piezoelectric Micromechanical Ultrasonic Transducer Based on Sc-Doped AlN Film," *Sensors*, vol. 22, no. 21, p. 8100, Oct. 2022, doi: 10.3390/s22218100.

[4] A. Savoia *et al.*, "Enhanced echographic images obtained improving the membrane structural layer of the cMUT probe," in *IEEE Ultrasonics Symposium, 2005.*, Sep. 2005, pp. 1960–1963. doi: 10.1109/ULTSYM.2005.1603259.

[5] A. Dangi *et al.*, "Ring PMUT array based miniaturized photoacoustic endoscopy device," in *Photons Plus Ultrasound: Imaging and Sensing 2019*, SPIE, Feb. 2019, pp. 46–53. doi: 10.1117/12.2510000.

[6] A. S. Savoia *et al.*, "Design, Fabrication, Characterization, and System Integration of a 1-D PMUT Array for Medical Ultrasound Imaging," in *2021 IEEE International Ultrasonics Symposium (IUS)*, Sep. 2021, pp. 1–3. doi: 10.1109/IUS52206.2021.9593751.

[7] J. Cai *et al.*, "Beyond fundamental resonance mode: high-order multi-band ALN PMUT for in vivo photoacoustic imaging," *Microsyst. Nanoeng.*, vol. 8, no. 1, Art. no. 1, Nov. 2022, doi: 10.1038/s41378-022-00426-7.

[8] J. Cai *et al.*, "Photoacoustic Imaging Based on Broadened Bandwidth Aluminum Nitride Piezoelectric Micromachined Ultrasound Transducers," *IEEE Sens. Lett.*, vol. 7, no. 4, pp. 1–4, Apr. 2023, doi: 10.1109/LSENS.2023.3254593.

[9] M. Sarafianou *et al.*, "A Novel Multi-Angle Spatial Compounding Methodology Toward High-Resolution PMUT-Based Imaging," *IEEE Sens. J.*, vol. 26, no. 7, pp. 9408–9421, Apr. 2026, doi: 10.1109/JSEN.2025.3572119.

[10] P. S. Balasubramanian, A. Singh, C. Xu, and A. Lal, "GHz Ultrasonic Chip-Scale Device Induces Ion Channel Stimulation in Human Neural Cells," *Sci. Rep.*, vol. 10, p. 3075, Feb. 2020, doi: 10.1038/s41598-020-58133-0.

[11] J. Lee *et al.*, "A MEMS ultrasound stimulation system for modulation of neural circuits with high spatial resolution in vitro," *Microsyst. Nanoeng.*, vol. 5, no. 1, Art. no. 1, Jul. 2019, doi: 10.1038/s41378-019-0070-5.

[12] H. J. Lee, N. Choi, E.-S. Yoon, and I.-J. Cho, "MEMS devices for drug delivery," *Adv. Drug Deliv. Rev.*, vol. 128, pp. 132–147, Mar. 2018, doi: 10.1016/j.addr.2017.11.003.

[13] S. Schoen *et al.*, "Towards controlled drug delivery in brain tumors with microbubble-enhanced focused ultrasound," *Adv. Drug Deliv. Rev.*, vol. 180, p. 114043, Jan. 2022, doi: 10.1016/j.addr.2021.114043.

[14] M. Saccher, A. S. Savoia, R. van Schaijk, J. H. Klootwijk, and R. Dekker, "Pre-Charged Collapse-Mode Capacitive Micromachined Ultrasonic Transducer (CMUT) Receivers for Efficient Power Transfer," *IEEE Trans. Ultrason. Ferroelectr. Freq. Control*, vol. 72, no. 2, pp. 283–297, Feb. 2025, doi: 10.1109/TUFFC.2024.3523179.

[15] A. I. Velea *et al.*, "Effects of Soft Encapsulation on the Receive Performance of PMUTs for Implantable Devices," *IEEE Trans.*

This article has been accepted for publication in IEEE Transactions on Ultrasonics. This is the author's version which has not been fully edited and
content may change prior to final publication. Citation information: DOI 10.1109/TUSON.2026.3722028

Ultrason. Ferroelectr. Freq. Control, vol. 72, no. 9, pp. 1282–1292, Sep. 2025, doi: 10.1109/TUFFC.2025.3592740.

[16] G.-L. Luo, Y. Kusano, and D. A. Horsley, “Airborne Piezoelectric Micromachined Ultrasonic Transducers for Long-Range Detection,” *J. Microelectromechanical Syst.*, vol. 30, no. 1, pp. 81–89, Feb. 2021, doi: 10.1109/JMEMS.2020.3037298.

[17] H. Yang *et al.*, “AlScN Film Based Piezoelectric Micromechanical Ultrasonic Transducer for an Extended Long-Range Detection,” *Micromachines*, vol. 13, no. 11, p. 1942, 2022, doi: 10.3390/mi13111942.

[18] M. Sarafianou *et al.*, “High-Precision Airborne Rangefinding with PMUTs Based on Signal Spatial Coherence,” in *2025 IEEE International Ultrasonics Symposium (IUS)*, Sep. 2025, pp. 1–4. doi: 10.1109/IUS62464.2025.11201514.

[19] D. J. Goh *et al.*, “A Convex PMUT Array for High-Speed Wide-FoV Airborne Object Sensing,” in *2025 IEEE International Ultrasonics Symposium (IUS)*, Sep. 2025, pp. 1–4. doi: 10.1109/IUS62464.2025.11201311.

[20] J. Liu *et al.*, “Sputtered PZT pMUT with Bias-Tunable Electromechanical Coupling Coefficient for Air-coupled Ranging Applications,” in *2022 IEEE International Ultrasonics Symposium (IUS)*, Oct. 2022, pp. 1–4. doi: 10.1109/IUS54386.2022.9958698.

[21] G. Giribaldi, B. H. Soukup, P. Simeoni, L. Colombo, and M. Rinaldi, “Matching-network boosting enabling reconfigurable pMUTs for IoT sensor node applications,” in *2022 IEEE International Ultrasonics Symposium (IUS)*, Oct. 2022, pp. 1–4. doi: 10.1109/IUS54386.2022.9957730.

[22] X. Li, J. Qian, J. Zhang, B. Zhang, J. E.-Y. Lee, and W. Zhang, “Piezoelectric Micromachined Ultrasonic Transducer Enables Bubble-Based Stirring and Reconfigurable Particle Patterning,” in *2023 22nd International Conference on Solid-State Sensors, Actuators and Microsystems (Transducers)*, Jun. 2023, pp. 903–906. Accessed: Mar. 20, 2026. [Online]. Available: https://ieeexplore.ieee.org/abstract/document/10517076

[23] W. Shang *et al.*, “Reconfigurable ScAlN Piezoelectric Micromachined Ultrasonic Transducer Arrays for Range Finding,” *Micromachines*, vol. 16, no. 2, Jan. 2025, doi: 10.3390/mi16020145.

[24] Y. Qiu *et al.*, “Piezoelectric Micromachined Ultrasound Transducer (PMUT) Arrays for Integrated Sensing, Actuation and Imaging,” *Sensors*, vol. 15, no. 4, pp. 8020–8041, Apr. 2015, doi: 10.3390/s150408020.

[25] K. Roy, J. E.-Y. Lee, and C. Lee, “Thin-film PMUTs: a review of over 40 years of research,” *Microsyst. Nanoeng.*, vol. 9, no. 1, Art. no. 1, Jul. 2023, doi: 10.1038/s41378-023-00555-7.

[26] J. Jung, W. Lee, W. Kang, E. Shin, J. Ryu, and H. Choi, “Review of piezoelectric micromachined ultrasonic transducers and their applications,” *J. Micromechanics Microengineering*, vol. 27, no. 11, p. 113001, Sep. 2017, doi: 10.1088/1361-6439/aa851b.

[27] Z. Liu, S. Yoshida, D. A. Horsley, and S. Tanaka, “Fabrication and characterization of row-column addressed pMUT array with monocrystalline PZT thin film toward creating ultrasonic imager,” *Sens. Actuators Phys.*, vol. 342, p. 113666, Aug. 2022, doi: 10.1016/j.sna.2022.113666.

[28] R. Miyake, M. Kiuchi, S. Yoshida, S. Tanaka, and G. R. Fox, “Commercial Production of Epitaxial PZT for Piezoelectric MEMS Applications,” in *2020 Joint Conference of the IEEE International Frequency Control Symposium and International Symposium on Applications of Ferroelectrics (IFCS-ISAF)*, Jul. 2020, pp. 1–3. doi: 10.1109/IFCS-ISAF41089.2020.9234898.

[29] P. Muralt *et al.*, “Piezoelectric micromachined ultrasonic transducers based on PZT thin films,” *IEEE Trans. Ultrason. Ferroelectr. Freq. Control*, vol. 52, no. 12, pp. 2276–2288, Dec. 2005, doi: 10.1109/TUFFC.2005.1563270.

[30] M. W. Hooker, “Properties of PZT-Based Piezoelectric Ceramics Between -150 and 250 C,” NAS 1.26:208708, Sep. 1998. Accessed: Mar. 27, 2026. [Online]. Available: https://ntrs.nasa.gov/citations/19980236888

[31] E. Lee, J. K. Lee, J. Lee, H. Jang, and S.-J. Kim, “Zr/Ti ratio dependence of the deformation in the hysteresis loop of Pb(Zr,Ti)O3 thin films,” *J. Mater. Sci. Lett.*, vol. 18, pp. 2025–2028, Dec. 1999, doi: 10.1023/A:1006797421070.

[32] S. Fichtner, N. Wolff, F. Lofink, L. Kienle, and B. Wagner, “AlScN: A III-V semiconductor based ferroelectric,” *J. Appl. Phys.*, vol. 125, no. 11, p. 114103, Mar. 2019, doi: 10.1063/1.5084945.

[33] Y. Birjis *et al.*, “Piezoelectric Micromachined Ultrasonic Transducers (PMUTs): Performance Metrics, Advancements, and Applications,” *Sensors*, vol. 22, no. 23, p. 9151, Nov. 2022, doi: 10.3390/s22239151.

[34] C. Liu, B. Varghese, P. P. Liu, H. Lin, M. Li, and Y. Zhu, “Measurement and Analysis of Longitudinal and Transversal Effective Piezoelectric Coefficients (d33,f and e31,f) in 100 nm-500 nm Sc0.3Al0.7N films,” in *2023 IEEE International Ultrasonics Symposium (IUS)*, Sep. 2023, pp. 1–4. doi: 10.1109/IUS51837.2023.10306779.

[35] M. Ji, H. Yang, Y. Zhou, X. Xiu, H. Lv, and S. Zhang, “Bimorph Dual-Electrode ScAlN PMUT with Two Terminal Connections,” *Micromachines*, vol. 13, no. 12, Art. no. 12, Dec. 2022, doi: 10.3390/mi13122260.

[36] Q. Wang, Y. Lu, S. Mishin, Y. Oshmyansky, and D. A. Horsley, “Design, Fabrication, and Characterization of Scandium Aluminum Nitride-Based Piezoelectric Micromachined Ultrasonic Transducers,” *J. Microelectromechanical Syst.*, vol. 26, no. 5, pp. 1132–1139, Oct. 2017, doi: 10.1109/JMEMS.2017.2712101.

[37] X. Liu *et al.*, “Multiphysics Modeling and Analysis of Sc-Doped AlN Thin Film Based Piezoelectric Micromachined Ultrasonic Transducer by Finite Element Method,” *Micromachines*, vol. 14, no. 10, Art. no. 10, Oct. 2023, doi: 10.3390/mi14101942.

[38] M. Sarafianou *et al.*, “Long-Range High-Resolution Imaging With Silicon-on-Nothing ScAlN pMUTs,” *IEEE Sens. J.*, vol. 23, no. 20, pp. 24254–24263, Oct. 2023, doi: 10.1109/JSEN.2023.3302354.

[39] H. Wang, N. Adamski, S. Mu, and C. G. Van de Walle, “Piezoelectric effect and polarization switching in Al1−xScxN,” *J. Appl. Phys.*, vol. 130, no. 10, p. 104101, Sep. 2021, doi: 10.1063/5.0056485.

[40] B. Herrera, M. Pirro, G. Giribaldi, L. Colombo, and M. Rinaldi, “AlScN Programmable Ferroelectric Micromachined Ultrasonic Transducer (FMUT),” in *2021 21st International Conference on Solid-State Sensors, Actuators and Microsystems (Transducers)*, Jun. 2021, pp. 38–41. doi: 10.1109/Transducers50396.2021.9495581.

[41] J. S. Park *et al.*, “Dual-frequency piezoelectric micromachined ultrasound transducer based on polarization switching in ferroelectric thin films,” *Microsyst. Nanoeng.*, vol. 9, no. 1, pp. 1–11, Oct. 2023, doi: 10.1038/s41378-023-00595-z.

[42] L. T. C, P. Kumar, S. Khan, and G. Pillai, “Novel Fabrication Scheme Using Lateral Stacking of Hybrid Piezo/Ferroelectric Thin-Films for MEMS Resonators,” in *2025 23rd International Conference on Solid-State Sensors, Actuators and Microsystems (Transducers)*, Jun. 2025, pp. 731–734. doi: 10.1109/Transducers61432.2025.11109822.

[43] C. Liu *et al.*, “Experimental Insights of ScAlN-Based Switchable Resonator and Filter: Operation and Reliability,” in *2025 IEEE International Electron Devices Meeting (IEDM)*, Dec. 2025, pp. 1–4. doi: 10.1109/IEDM50572.2025.11353622.

[44] J. Liu *et al.*, “Transmit-Receive Performance Enhancement of Sc0.3AL0.7N Pmuts Through Ferroelectric Activation,” in *2026 IEEE 39th International Conference on Micro Electro Mechanical Systems (MEMS)*, Jan. 2026, pp. 770–773. doi: 10.1109/MEMS64181.2026.11419481.

[45] Y.-Y.-S. Cheng *et al.*, “Large linear high-frequency strain by interlocked monoclinic polar nanoregions,” *Nat. Mater.*, vol. 25, no. 1, pp. 73–79, Jan. 2026, doi: 10.1038/s41563-025-02354-z.

[46] H. Lin *et al.*, “Effect of Polarity Switching on the Effective Piezoelectric Coefficient of Sc0.3Al0.7N Bilayer,” in *2025 IEEE International Ultrasonics Symposium (IUS)*, Sep. 2025, pp. 1–4. doi: 10.1109/IUS62464.2025.11201749.

[47] C. Liu *et al.*, “Clamping Effect of Dielectric and Ferroelectric Properties in ScAlN,” in *2024 IEEE Ultrasonics, Ferroelectrics, and Frequency Control Joint Symposium (UFFC-JS)*, Sep. 2024, pp. 1–4. doi: 10.1109/UFFC-JS60046.2024.10793920.

[48] Y. Gu *et al.*, “Mutable Polarization Switching Characteristics in Wurtzite Al1-xScxN Ferroelectric Films Enabled by Sc-Doping,” *Small*, vol. 21, no. 34, 2025, doi: 10.1002/smll.202502865.

[49] J. Huang *et al.*, “Atomistic Structure of Transient Switching States in Ferroelectric AlScN,” *Phys. Rev. Lett.*, vol. 136, no. 2, p. 026801, Jan. 2026, doi: 10.1103/lfdh-86x6.

[50] N. Wolff *et al.*, “Electric field-induced domain structures in ferroelectric AlScN thin films,” *J. Appl. Phys.*, vol. 137, no. 8, p. 084101, Feb. 2025, doi: 10.1063/5.0244102.

[51] N. Wolff *et al.*, “Interfacial Polarization Switching in Al0.92Sc0.08N/GaN Heterostructures Grown by Sputter Epitaxy,” *Adv. Sci.*, vol. 12, no. 30, 2025, doi: 10.1002/advs.202503827.

[52] J. Wang *et al.*, "Unveiling interfacial dead layer in wurtzite ferroelectrics," *Nat. Commun.*, vol. 16, no. 1, 2025, doi: 10.1038/s41467-025-61291-2.

[53] S. Calderon, C. Skidmore, J.-P. Maria, and E. C. Dickey, "Domain Nucleation and Growth in an Epitaxially Grown Wurtzite Ferroelectric," *Adv. Funct. Mater.*, vol. 36, no. 2, 2026, doi: 10.1002/adfm.202510493.

[54] Y. Yang *et al.*, "Thickness-Driven Transition of Switching Kinetics in Wurtzite Ferroelectrics," *Adv. Funct. Mater.*, vol. 36, no. 11, 2026, doi: 10.1002/adfm.202511380.

[55] J. Wang *et al.*, "Unveiling interfacial dead layer in wurtzite ferroelectrics," *Nat. Commun.*, vol. 16, no. 1, p. 6069, Jul. 2025, doi: 10.1038/s41467-025-61291-2.

Sean J.Z. Wong started his PhD at the National University of Singapore in 2022, as a continuation of his B.S degree in mechanical engineering. His background is in robotics, control systems, and artificial intelligence, and is currently branching out to microelectronics, MEMS devices, ultrasound transducers, and biomedical applications as part of his PhD research and future goals. He is currently under the A*STAR Graduate Scholarship with the Institute of Microelectronics, A*STAR, Singapore. His future research is aimed to be in the areas of micro-robotics, robot actuation systems, and artificial intelligence.

Chen Liu received his B.E. degree in Peking University, Beijing, China, in 2014, and the Ph.D. degree in School of integrated circuits, Peking University, Beijing, China, in 2019. He joined the Institute of Microelectronics (IME), Agency for Science, Technology and Research (A*STAR), Singapore since 2019, and currently is a senior scientist and a principal investigator in Micro Electro Multiphysics Systems (MEMS) Department, where he is leading the development of next-generation radio-frequency filters and non-volatile memories. His research interests include the piezoelectric and ferroelectric materials, piezoelectric MEMS devices and emerging non-volatile memories.

Hong Yan is a Lead Research Engineer at the Institute of Microelectronics (IME), A*STAR, Singapore, focusing on MEMS process integration with piezoelectric materials. She has more than 20 years of experience across major semiconductor foundries, including ASMC (Shanghai, China), GlobalFoundries (Singapore), and Hongli Semiconductor (Shanghai, China). She has extensive experience supporting pilot-line and manufacturing environments through process optimization, characterization, and close collaboration with integration, equipment, and manufacturing teams.

Muhammad U. Khan was born in Rawalpindi, Punjab, Pakistan, in 1995. He received his B.S. degree in Mechatronics Engineering from the University of Engineering and Technology, Taxila, Punjab, Pakistan, in 2018, and his M.S. degree in Mechatronics Engineering from the College of Electrical and Mechanical Engineering, National University of Sciences and Technology (NUST), Islamabad, Pakistan, in 2022. Since 2023, he has been pursuing his Ph.D. in the Department of Industrial, Electronic, and Mechanical Engineering of Roma Tre University, Rome, Italy. His primary research interests lie in the characterization of micromachined ultrasonic transducers (MUTs). He is currently involved in developing novel characterization techniques for micromachined ultrasonic transducers (MUTs).

Chengkuo Lee (SM'19) received his Ph.D. degree from The University of Tokyo in 1996. Currently, he is the GlobalFoundries Chair Professor and director of the Center for Intelligent Sensors and MEMS (CISM) at National University of Singapore, Singapore.

Alessandro Stuart Savoia (M'04) received the Ph.D. degree in Electronic Engineering from Roma Tre University, Rome, Italy, in 2007. From 2008 to 2010, he was co-founder and R&D Manager of an academic spin-off company of Roma Tre University, focused on the industrial exploitation of MEMS-based ultrasonic transducers. He is currently a Professor of Electronics with the Department of Industrial, Electronic, and Mechanical Engineering, Roma Tre University. His research interests include the development and system integration of MEMS ultrasonic transducers, including electrostatic (CMUT) and piezoelectric (PMUT) devices. Dr. Savoia served the IEEE UFFC Society as an Associate Editor for the IEEE Transactions on Ultrasonics, Ferroelectrics, and Frequency Control, and as Chair of Technical Program Committee Group 5, "Transducers and Transducer Materials," for the IEEE International Ultrasonics Symposium.

Yao Zhu is the Head of MEMS department in Institute of Microelectronics (IME), A*STAR Singapore. Her current research interests include MEMS devices for sensing, actuating and wireless communication applications. Zhu Yao received her Ph.D. degree from Nanyang Technological University in 2015. She is actively involved in IEEE societies such as associate editor for IEEE MEMS Journal, committee member of IEEE Solid State Circuit Society Singapore Chapter & IEEE Nanotechnology Technical Council, technical sub-committee member of IEEE IEDM 2023 and IEEE MEMS 2023. She is the recipient of SEMI MEMS & Sensors Industry Group Emerging Leaders Awards 2022.